SenSARS: A Low-Cost Portable Electrochemical System for Ultra-Sensitive, Near Real-Time, Diagnostics of SARS-CoV-2 Infections

Sammy A. Perdomo⬤, Viviana Ortega⬤, Andres Jaramillo-Botero⬤, Nelson Mancilla⬤,
José Hernando Mosquera-DeLaCruz⬤, Drochss Pettry Valencia⬤, Mauricio Quimbaya⬤, Juan David Contreras⬤,
Gabriel Esteban Velez⬤, Oscar A. Loaiza⬤, Adriana Gómez⬤, and Jhonattan de la Roche⬤

Abstract—A critical path to solving the SARS-CoV-2 pandemic, without further socioeconomic impact, is to stop its spread. For this to happen, pre- or asymptomatic individuals infected with the virus need to be detected and isolated opportunely. Unfortunately, there are no current ubiquitous (i.e., ultra-sensitive, cheap, and widely available) rapid testing tools capable of early detection of SARS-CoV-2 infections. In this article, we introduce an accurate, portable, and low-cost medical device and bio-nanosensing electrode dubbed SenSARS and its experimental validation. SenSARS' device measures the electrochemical impedance spectra of a disposable bio-modified screen-printed carbon-based working electrode (SPCE) to the changes in the concentration of SARS-CoV-2 antigen molecules ("S" spike proteins) contained within a sub-microliter fluid sample deposited on its surface. SenSARS offers real-time diagnostics and viral load tracking capabilities. Positive and negative control tests were performed in phosphate-buffered saline (PBS) at different concentrations (between 1 and 50 fg/mL) of SARS-CoV-2(S), Epstein–Barr virus (EBV) glycoprotein gp350, and Influenza H1N1 M1 recombinant viral proteins. We demonstrate that SenSARS is easy to use, with a portable and lightweight (<200 g) instrument and disposable test electrodes (<U.S. $5), capable of fast diagnosis (∼10 min), with high analytical sensitivity (low limits of detection, LOD = 1.065 fg/mL, and quantitation, LOQ = 3.6 fg/mL) and selectivity to SARS-CoV-2(S) antigens, even in the presence of structural proteins from the other pathogens tested. SenSARS provides a potential path to pervasive rapid diagnostics of SARS-CoV-2 in clinical, point-of-care, and home-care settings, and to breaking the transmission chain of this virus. Medical device compliance testing of SenSARS to EIC-60601 technical standards is underway.

Index Terms—Biosensors, electrochemical biosensors, electrochemical impedance spectroscopy (EIS), SARS-CoV-2.

I. Introduction

THE world is experiencing one of the worst historically recorded public health crises [1], one that threatens human existence and our way of life as a whole [2]. The socioeconomic impacts caused by the appearance of the SARS-CoV-2 virus are not yet fully quantified [3]. The worldwide outbreak of the COVID-19 disease, caused by this virus, has spurred a response like few others from the scientific community, a race to find effective and innovative solutions to stop its spread [4]. SARS-CoV-2's high pathogenicity continues to wreak havoc, with thousands of people worldwide still dying and a significantly higher number being infected per day [5].

The advent of effective vaccines has brought some relief, albeit improved diagnostic, prophylactic, and therapeutic solutions are still sorely needed, especially considering a large portion of the world's population remains unvaccinated. For diagnostics, rapid and early detection tools for selective identification of pre, asymptomatic, and symptomatic individuals infected with SARS-CoV-2 remains a top priority, one that will contribute to breaking the chain of transmission [5], [6].

Current diagnostic tests for SARS-CoV-2 include nucleic acid, antibody, and protein-based detections, with viral nucleic acid detection by reverse transcriptase–polymerase chain reaction (RT–PCR) as the "golden standard" [7]. Real-time RT-PCR technologies offer high sensitivity and detection specificity, with 2–3 h for diagnosis. They require extensive sample manipulation, isolation, and amplification of the virus' genetic material, as well as the use of expensive instrumentation, both of which restrict ubiquitous use and effective control strategies to limit infections [8]. Real-time RT-PCR diagnostics tools are capable of detecting the genetic material of the virus in a human host approximately 4–5 days after infection, but due to costs (U.S. $100–200), their prophylactic use is limited to a fraction of those infected [9].

Today, a wide range of alternative technologies to RT-PCR are available to diagnose viral diseases, including immunoassays [10], [11], and immunoreaction-based biosensors [12]. Immunoassays measure the presence of an analyte in solution through the use of antibodies or antigens, by producing a mea-
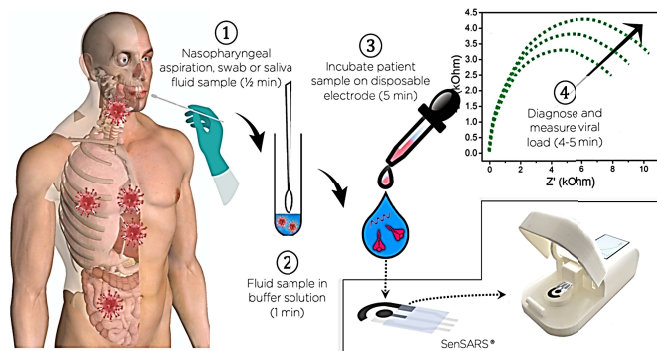
Fig. 1.   Stepwise antigen-based diagnostics protocol in SenSARS. The lower right outlined inset figure shows the two main components in SenSARS, an SPCE (left) and a portable electrochemical impedance spectrometer (right). Human figure generated with iOS, Essential Anatomy 5 (https://3d4medical.com).
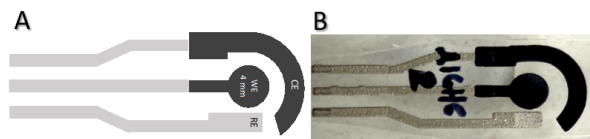

Fig. 2.   (a) Layout of screen-printed carbon electrodes (SPCEs) used in this work includes a WE and a CE made of carbon paste and the RE from Ag/AgCl, as well as the grey terminal contacts. The electrodes are partially protected with an insulating dielectric layer (ESL ElectroScience Europe, U.K., ESL 4917). Each SPCE measures $1 \times 0.5''$. (b) SPCE photograph. SPCEs reported here were fabricated at the Universidad del Valle facilities.

surable signal in response to the binding of an antibody to its antigen. Immunoreaction-based biosensors have recently been demonstrated on SARS-CoV-2 diagnosis [13], including electronic field-effect currents [14], surface plasmon energies [15], optical shifts [15], electrochemical processes [16]–[20], piezoelectric [21], or thermal [15]. Unfortunately, most remain at a low technology readiness level (TRL < 4) or are limited by poor production scalability.

Immunoreaction-based biosensors allow the detection of target analytes in solution at very low concentrations ($<$nM/L) [22], [23]. They consist of three main elements: a biologically modified electrode, a transducer, and a signal processing element. The biologically modified electrode/receptor is used to selectively capture analytes on an electroactive material. The transducer then transforms the signal resulting from the analyte's interaction with the electrode's surface into a signal that can be measured and quantified, e.g., physicochemical, electrochemical, field-effect, optical, and piezoelectric. The signal processing element is then used to adjust the units of measurement and present the results in a user-friendly fashion.

In this article, we describe an antigen-based technology, dubbed SenSARS (see Fig. 1), which involves an antibody-modified screen-printed carbon working electrode (SPCE) on a polyethylene terephthalate (PET) substrate, in a planar three-electrode electrochemical cell configuration, and a microcontroller-based processing and interface unit. The electrochemical transducer converts the redox reactions from an electroactive species occurring on the surface of the bio-modified SPCE into a change in impedance, which in turn correlates directly and accurately with the concentration of selectively adsorbed antigen molecules from a fluid sample on the electrode's surface. SenSARS includes a portable impedance spectrometer with a minimum of 5-h operational autonomy in a small and light form factor unit ($<$200 g) capable of ultra-sensitive measurement (1 fg/mL limit of detection, LOD) of spike protein concentrations from a sub-μL sample of fluid and a fast time to diagnosis ($\sim$10 min).

The rest of this article covers the design and implementation (Section II), characterization, testing, and validation results (Section III) of SenSARS' different components (depicted in the lower right inset of Fig. 1). Section IV summarizes the relevance and potential impact of SenSARS.

II. MATERIALS AND METHODS

A. Fabrication and Functionalization of SenSARS' SPCEs

The SPCEs are fabricated using a screen-printing thick-film deposition process [24]. The three-electrode configuration consists of a working electrode (WE with 4.4 mm diameter), an Ag/AgCl pseudoreference electrode [25] (RE, 0.302 V versus a normal hydrogen electrode), and a counter electrode (CE) printed in an interdigitated layout over a PET film substrate (shown in Fig. 2).

The thick-film screen-printing process involved depositing one layer of carbon ink and one layer of Ag/AgCl ink for all three electrodes, as shown in Fig. 2. In all, 132 SPCEs were printed on a standard A4 format PET sheet, and a total of 15 sheets were produced from a single batch (1980 total).

SPCEs with end-point ohmic resistance $<$300 Ω in each of the three electrodes per SPCE were preselected for this work. Each electrode was then cleaned using a swab impregnated with analytical grade methanol (with no pressure applied). Two cyclic voltammetry (CV) scans at a rate of 0.05 V/s and a potential amplitude of 10 mV and a electrochemical impedance spectroscopy (EIS) test from 0.02 Hz to 20 kHz with 53 points and the same voltage amplitude were then performed with a Palmsens4 potentiostat/galvanostat (from Palmsens) on each SPCE to confirm a quasi-reversible behavior toward active redox species, using 50 μL of $K_3Fe(CN)_6$ in PBS 1X solution. SPCEs with value of charge transfer resistance (R_{ct}) < 5000 Ω were chosen for bio-functionalization in this work, for predevelopment optimization and final testing.

The WE and CE were printed using DuPont's BQ221 carbon-based conductive paste (DuPont, USA) and cured at 130 °C for 10 min. The RE is screen-printed using DuPont's 5874 Ag/AgCl paste (DuPont, USA), with an Ag:AgCl ratio of 65:35, and dried at 120 °C for 5 min.

The surface of the WE was modified for the selective detection of SARS-CoV-2 spike protein. This involved electrodeposition of para-aminobenzoic acid (PABA) on the WE's carbon surface, via 50 μL of diazonium salt solution, diluted in HCl 0.1 M, over all three electrodes (WE, RE, and CE). PABA consists of a benzene ring substituted with amino and carboxyl groups in the para position.

We then applied CV sweeps between -0.2 and 0.6 V at a rate of 0.1 V/s with the Palmsens4 potentiostat, until no irreversible reduction peaks were observed ($<$5 cycles). Reduction peaks indicate the electro-reduction band of the diazonium salt on the surface carbon atoms and the production of a radical aryl. This dissociates the amino group
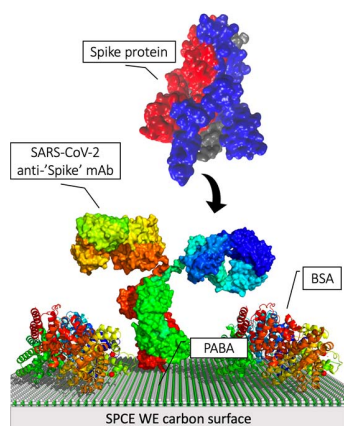
Fig. 3.   Molecular model schematic of the WE's modified surface (PABA, mAb(S), BSA) and an approaching "spike" glycoprotein onto the antibody binding domain.

from the PABA and promotes grafting of the aryl radical to the carbon substrate. The PABA-modified WEs were then washed with type 1 water and dried under a cold air stream. The PABA was then chemically activated with 1-ethyl-3-(3-dimethylamino propyl) carbodiimide hydrochloride (EDC). EDC reacts with the carboxylic groups to form an active O- intermediate. N-hydroxysuccinimide (NHS) was added to increase the efficiency of EDC reactions. A solution of monoclonal antibody (mAb) dissolved in phosphate-buffered saline (PBS 1X, 0.01 M at pH 7.4) was then incubated for 2 h on the WE. Reference 4015-D003 chimeric Anti-Spike-mAb from Sinobiological was used for spike protein selectivity.

We accelerated the EDC-sulfo(NHS) activation process with 2-(N-morpholino)ethanesulfonic acid (MES). mAbs bind to the carboxyl end of PABA, preferentially through their lysine residues. The SPCE was then washed with 5 mL of PBS 1X solution and dried at room temperature.

To passivate the carboxylic vacancies from the PABA, a 1% concentrated solution (10 mg/mL) of bovine serum albumin (BSA) was dissolved in a sodium salt (0.5 M MES) buffer solution at pH 6.0 and incubated on the WE for 1 h at room temperature. The SPCE was then washed again with 5 mL of PBS 1X solution and dried at room temperature, before use or preservation in a 4 °C humid environment. A molecular representation of the functionalized electrode surface is shown in Fig. 3. Sample CV tests performed at each functionalization stage with Palmsens4 potentiostat/galvanostat are included in Fig. S1 of the supplementary information (SI).

We characterized each SPCE using EIS and obtained a nanoscale morphological view of the different modification stages from multiple sites of a single WE, using a Cypher-ES atomic force microscope (AFM) from Asylum Research. These results are described in Sections II-C and III-A.

B. SenSARS' EIS Instrument

Fig. 4 depicts a block diagram representation of SenSARS' device architecture. It uses a Raspberry Pi 4B single-board computer, with a Broadcom BCM2711 Quad-Core Cortex-A72 64 bits processor running at a frequency of 1.5 GHz,
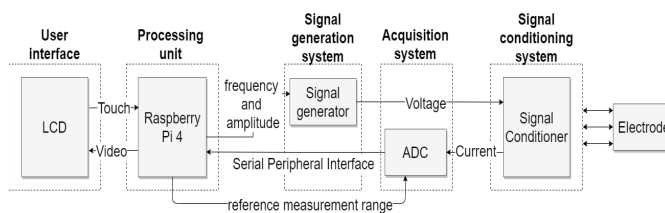

Fig. 4.   Block diagram of SenSARS' hardware architecture. The signal generation system produces the sinusoidal waveform that is applied to the SPCEs. The signal conditioning module is responsible for amplifying, filtering, and converting the current signal measured through the WE into an equivalent potential that is digitalized by the acquisition module and relayed to the data processing module where the EIS and diagnostics algorithms are executed.

TABLE I
SIGNAL GENERATION MODULE SPECIFICATIONS

Parameters	Value
Peak amplitude range	10 mV – 1.6 V
Frequency range	0.5 Hz – 10 kHz
Output current range	2 nA – 3 mA
Voltage supply	5 V

a 2-GB LPDDR4 RAM, a 2.8″ resistive LCD touch screen with 320 × 240 pixels resolution (DFR0275), an integrated XR2206 waveform generation module capable of producing sine, square, and triangular waveforms, over a frequency range between 0.5 Hz and 1 MHz, a signal acquisition module with a digital-to-analog conversion (DAC) unit, and an operational amplifier circuitry for signal conditioning and filtering. Power is supplied by an Alongza USB 5-V charging module with a 5000-mAh capacity, which delivers 5 h of continuous operation ($\sim$37 tests, with an average time of 8 min per EIS), a DC–DC converter producing 12- and -8:8-V sources [Fig. 5(a)]. We used the -8-/8-V range to power the XR2206 signal generator, following the datasheet recommendations, and the operational amplifier circuitry considering the output current range shown in Table I. The 5-V source is used to power the Raspberry unit and digital components. The 0–3.3-V electronics will be used in a next version of the instrument, to reduce its overall power consumption. The electronic specifications for the signal generator module are summarized in Table I; it uses an XR2206 monolithic function generator integrated circuit (IC) at its core. Table II summarizes the resistance and capacitance values that control the system's frequency range, between 0.5 Hz and 10 kHz, enabled via the XR2206 with resistance and capacitance values digitally controlled by the Raspberry Pi unit.

The resistors that control the frequency and amplitude, and the capacitance that sets the working frequency range, were replaced by digital potentiometers (DS1809-10 10 kΩ and DS1809-100 of 100 kΩ) and by a digitally controlled capacitors, respectively. This enabled software-based parameterization of the waveform signal's frequency and amplitude. The switched capacitor network is controlled by a 74hc4066 IC, via the CPU. Fig. 5(b) illustrates the circuit schematic of the signal generation module.

The signal conditioning module adjusts the offset (0 V) to compensate for the open-circuit potential and the $\pm$ signal

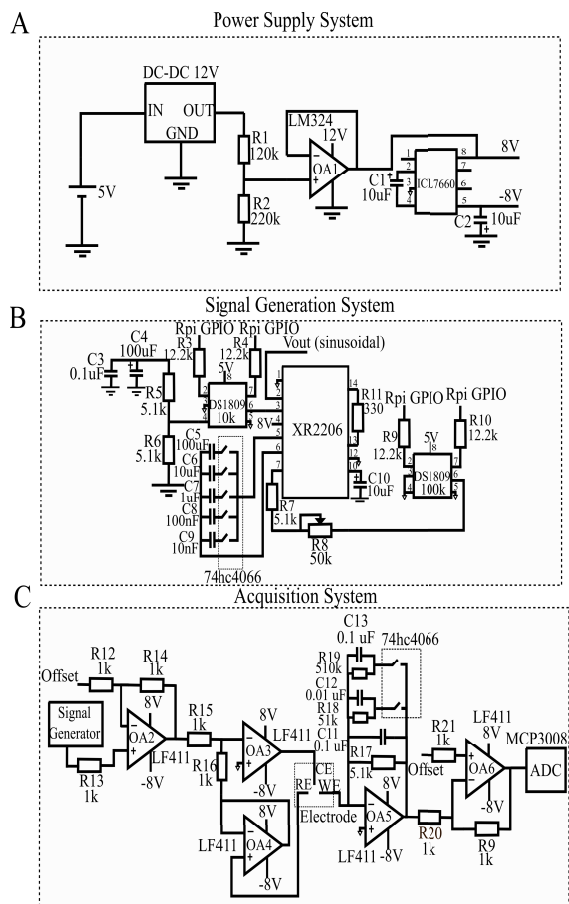| Frequency range	Capacitance	Resistance
0.1 − 1 Hz	100 uF	
1 − 10 Hz	10 uF	
10 − 100 Hz	1 uF	100 kΩ
100 − 1 kHz	100 nF	
1 k − 10 kHz	10 nF	

Fig. 5. (a) Schematic of the power supply circuit in SenSARS' device. The operational amplifier OA1 provides a voltage follower configuration to isolate the 5- and 8-V sources. (b) Electrical diagram of the signal generation module using the XR2206 IC. The DS1809 potentiometers are driven by the Raspberry PI unit to enable user control of the excitation waveform frequency and amplitude. The capacitors are selected by analog switches from 74hc4066, controlled by the Raspberry Pi unit. (c) Schematic of the signal conditioning module. Amplifiers OA2 and OA6 are responsible for shifting the dc level of the generated signal. The first one takes the offset of the generated sinusoidal signal to 0 V to apply the full potential range on the electrode through amplifiers OA3 and OA4. The second is responsible for recovering the original DC of the input signal.

amplitudes and then applies the potential waveforms produced by the signal generation module to the WE and amplifies and filters the current through the WE [26]. Fig. 5(c) provides a schematic diagram of the signal conditioning module. It includes a potentiostat to maintain a constant potential between RE and CE and to decouple electrodes [27]–[29]. The operational amplifiers act as buffers for each electrode. Here, the LF411 JFET-based operational amplifier allows for high input impedance and low input noise current. With the need to capture ultra-low analyte concentrations (<fg/mL),

with currents in the nA range, we use a trans-impedance amplifier (TIA) [30]–[33] that provides the current ranges specified in Table I, while filtering adherent noise [34]. These current ranges can be controlled with the analog switch 74hc4066 using the Raspberry. Currents above these ranges are limited (saturated) by the dual ±8-V potential and the low feedback resistance implemented in the TIA operational amplifier. The latter stage in the conditioning module incorporates a 10-bit MCP3008 DAC unit capable of sampling at 100 ks/s that discretizes the generated waveforms and the output current from the SPCE. Here, the offset of the output signal from the TIA stage must be adjusted to span it within the range of 0–3.3 V allowed by the DAC.

C. Electrochemical Characterization of the We

All SPCEs reported here were characterized via EIS [35] using SenSARS. CV characterization during the intermediate functionalization stages of the WE was performed using a Palmsens4 instrument. Impedimetric measurements were carried out after depositing 50 μL of $K_3Fe(CN)_6$ in PBS 1X solution over all three electrodes. Impedance measurements were performed at the equilibrium potential of the $[Fe(CN)_6]^{-4}/[Fe(CN)_6]^{-3}$ redox couple with a $V(t) = 0.01$ V (RMS) sinusoidal excitation amplitude. Measurements were made at 40 steps per decade in the appropriate frequency range, five times at each frequency, and averaged during each run. The impedance (Z) is expressed in terms of a real (Z') and an imaginary ($-Z''$) component. On an unmodified WE, the route to its surface is not blocked and the redox probe easily undergoes the alternating reactions induced by the driving ac voltage, $V(t)$.

At each modification step of the WE (4-PABA, mAb, and BSA) and during the testing of SARS-CoV-2(S) antigens, the ions in the redox probe will become increasingly blocked by bound molecules, leading to an increase in the charge transfer resistance (R_{ct}) of the interface. The WE impedance is affected by the biological layers that modify its surface. This effect is captured in a real versus imaginary impedance Nyquist plot [Fig. 6(a)], using an ac excitation signal of 10 mV in amplitude, over the frequency range of 0.5 Hz to 10 kHz. These parameters were selected to: 1) improve the measurement speed and response time of the EIS test ensuring that all critical data are recorded and 2) produce an interpretable EIS response minimizing the effect of noise [36].

Each resulting EIS was parameterized via a Randles equivalent electrical circuit model [30] [Fig. 6(b)] to describe the biosensor–liquid interface, using 50 μL of 1-mM solution of $K_3Fe(CN)_6$/PBS 1X.

To test the biomodified SPCEs in the laboratory, we prepared sample solutions of recombinant SARS-CoV-2 spike protein at different concentrations, from 1 to 100 fg/mL, in PBS 1X and incubated 0.3 μL of this mixture on the WE's surface at 5 $\pm$ 0.5 °C for 5 min, before recording an EIS. The EIS is used to determine the concentration of adsorbed spike proteins on the anchored mAbs. We established a positive infection threshold above 10% of the measured R_{ct}, to that of the blank SPCE (i.e., up to BSA layer). SenSARS' data
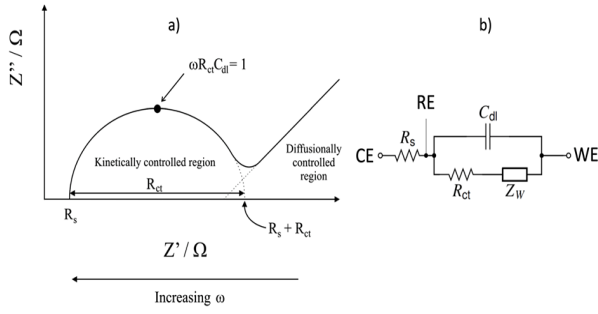
Fig. 6. (a) Parameters associated with a typical EIS (adapted from [37]). (b) Equivalent Randles electronic model of our SPCE's electrochemical cell. The measured opposition of the bio-functional layer to electric current flow under the alternating voltage signal, i.e., the impedance, is used to extract its charge transfer resistance (R_{ct}) across the biological layer. By fitting the curve obtained from the Nyquist plot to an equivalent Randles electrical circuit model, we extract R_{ct} as the difference between the maximum projected real impedance and the minimum starting real impedance, which corresponds to the ionic solvent's resistance (R_s).
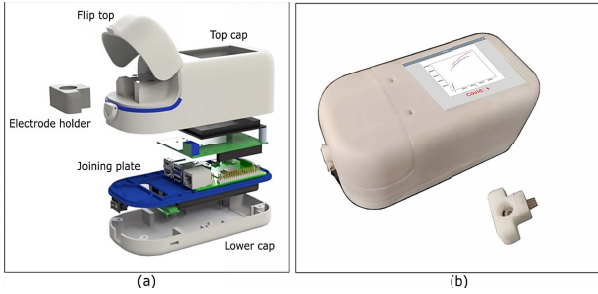

Fig. 7. (a) Exploded view of SenSARS portable device. (b) Photograph of the physical instrument and SPCE on a holder.

processing unit computes the impedance at each frequency over the specified range, using Ohm's law

$$Z = \frac{V}{I} e^{i\Gamma} \tag{1}$$

where Γ corresponds to the phase difference between the generated voltage (V) and the measured current (I). The real and imaginary components of the impedance (Z) in (1) are then derived from Euler's identity, as

$$Z' = \frac{V}{I}\cos\Gamma, \quad Z'' = \frac{V}{I}\text{sen}\Gamma \tag{2}$$

where the impedance tuple $[Z', Z'']$ represents a frequency point in the Nyquist plot (as shown in Fig. 6).

D. SenSARS' Enclosure

A plastic enclosure supports and protects the electronic circuitry. It includes an SPCE docking bay to avoid sample cross-contamination with a Faraday cage to protect low-current measurements from electromagnetic interference (EMI) and a touch screen interface to improve user control and monitoring [see Fig. 7(b)]. A reusable SPCE silicone sandwich support with an integrated fluid funnel allows safe measurements and secure disposal of the SPCE. The flip-top shown in Fig. 7(a) seals the SPCE's Faraday cage during EIS recording.

E. EIS Algorithm and Diagnostic Interface

SenSARS' touch screen interface provides two options, one to characterize a blank electrode and one to characterize a
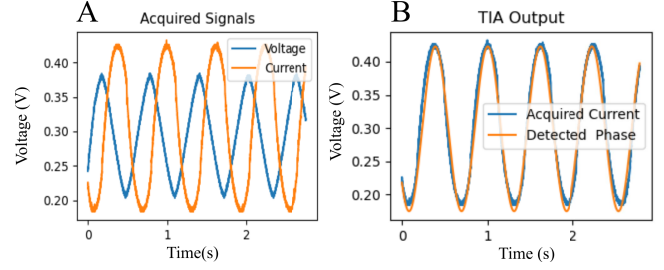

Fig. 8. Example signals acquired and processed by SenSARS' EIS instrument. (a) Voltage and current signals (amplified by the IxR value of the TIA) filtered with a median filter. (b) Estimated output phase (orange).
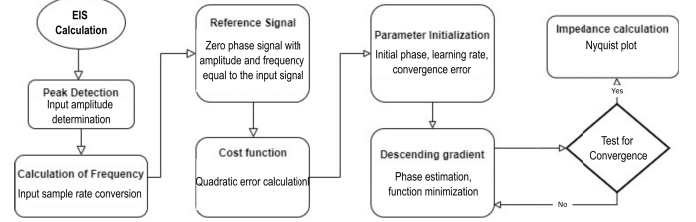

Fig. 9. Flowchart for the calculation of the EIS in each SPCE characterization. The total processing time between generation, acquisition, and visualization of the result is approximately 10 min.

loaded electrode. In each case, the unit verifies the presence of an SPCE in the docking bay, before applying the sinusoidal excitation potential between the WE and the RE and recording the output current flow. All input signals are digitally filtered to reduce noise [Fig. 8(a)]. The CPU calculates the impedance for each applied frequency, as described by (1) and (2). We use the steepest descent (SD) optimization algorithm to determine the phase difference between the applied potential and the output current. The amplitude and dc offset for each signal is calculated on the fly, thus only requiring the optimization of the waveform phase shift via SD. The root-mean-square (rms) error between the acquired signal, which changes in phase, and a reference sinusoidal signal at the same frequency and amplitude is used as a fitness function [Fig. 8(b)].

SenSARS calculates real and imaginary impedances from (2) over the range of frequencies. Impedance tuples are used to generate the corresponding Nyquist plot. The EIS macro-algorithm is described in Fig. 9.

The graphical user interface (GUI) was developed using the Python TKInter library and consists of the following routines: test type selection (unloaded electrode and loaded electrode characterization), a digital keyboard for correlating patient and electrode IDs, EIS graphing, and diagnostics based on the automated extraction of the R_{ct} difference between the loaded and unloaded SPCE EIS' (automatically extracted from the Randles equivalent circuit model fit). The unloaded SPCE EIS is recorded and stored after biomodification for each SPCE.

III. EXPERIMENTAL RESULTS

A. Nanoscale We Surface Morphology Characterization

To physically confirm the biofunctionalization of the WE, AFM height and phase images were obtained after each functionalization step for two different WEs, using a silicon FS-1500 AFM tip over randomly chosen regions of 0.5×0.5 μm^2 in noncontact (tapping) repulsive mode, for

the bare WE and the PABA-modified layer, and in a noncontact attractive mode for antibody and BSA layers to prevent mechanical damage to the biomodified WE surface. Roughness parameters were estimated by analyzing the topography scans of the dry WE's surface at each stage. The percent changes, from the bare to the PABA-modified surfaces, for ten different regions in both electrodes in terms of average roughness (R_a), rms roughness (R_q), and peak to valley height (H_t) were $\langle\Delta R_q\rangle = 55\%$, $\langle\Delta R_a\rangle = 55\%$, and $\langle\Delta H_t\rangle = 52\%$, respectively (see Fig. S2 of the SI). This indicates a ballistic growth model (BD) [38], consistent with filling of grain interstitials and an otherwise homogeneous layer deposition. Changes in the phase space between valley and cusp regions of the surface were also observed. These are attributed to the difference in the mechanical properties of the softer bio-materials deposited and the harder carbon substrate, as reported in the literature [39], [40]. Lesser changes in the surface roughness of the WEs were observed after incubating the mAb ($\langle\Delta R_q\rangle = 25\%$, $\langle\Delta R_a\rangle = 24\%$, $\langle\Delta H_t\rangle = 31\%$), albeit an increase in phase space contrast was observed at the grains' boundaries. This confirms anchoring of the mAb onto the activated carboxylic PABA groups, primarily within the interstitial regions. Antibodies covered ∼5.42% of the WE electrode surfaces, which is consistent with the findings from Nidzworski *et al.* [41]. Surface roughness parameters did not change significantly after incubating the final BSA layer (<5% for all parameters), yet there was an increase in phase space contrast at the inter-grain boundaries, commensurate with the additional organic material deposition. These results point to a higher electroactivity in the interstitial regions of the screen-printed carbon phases, which in turn facilitate chemical bio-functionalization. Images in Fig. S2 of the supplemental information provide additional visual insights into the nature of the deposited layers, including evidence of an antibody lying flat on a WE surface (inset Fig. S2C), similar to that reported by Orlando *et al.* [42], with a slightly larger footprint (12–20 nm along the mAb's Fc axis) than expected from the crystallographic information [43]. Noise and distortion in these images are attributed to denaturing of the protein by the AFM's probe [44].

B. SPCE Electrochemical Characterization

To confirm the accuracy of our results, obtained with SenSARS, we performed EIS experiments with a fixed reference Randles equivalent circuit [see Fig. 10(a)]. The dummy cell consists of $R1 = 10.2$-Ω and $R2 = 9.9$-Ω resistors in series with the parallel arrangement of $C1 = 100$ μF capacitor and $R3 = 98.9$-Ω resistor. To further validate the agreement of the EIS plots obtained with SenSARS and two commercial potentiostats (a PalmSens4 from Palmsens and an Autolab PGSTAT128N unit from Metrohm), under equal settings (Table I), we calculated a theoretical EIS with the corresponding Randles circuit using the EIS Spectrum Analyser software [52] [Fig. 10(b)]. The values for R1-3 and C1 were selected to validate all instruments for a small R_{ct} and small double-layer capacitance, where signal variance becomes more demanding for all instruments. The results show an R^2 of 0.9208 between SenSARS-Simulation, 0.8681
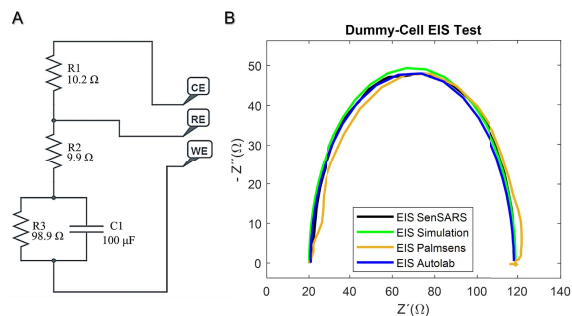

Fig. 10. EIS test of SenSARS on a dummy-cell circuit. (a) Implemented dummy cell circuit with electrodes' configuration. (b) EIS responses' comparison between all the instruments and the Randles simulation.
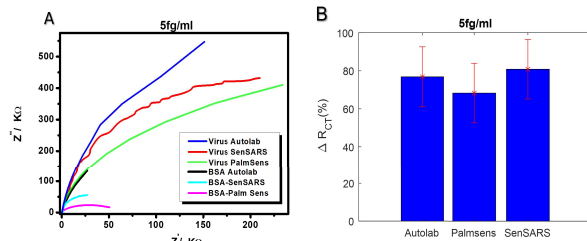

Fig. 11. SenSARS' EIS validation. (a) EIS comparison between SenSARS, Palmsens4, and Autolab's PGSTAT128N for a WE reference to BSA and the same electrode's response with SARS-CoV2 spike protein (Sinobiological ref 40591-V08H Spike S1-His Recombinant Protein) at a concentration of 5 fg/mL. (b) Relative ΔR_{ct} values' comparison for each EIS obtained on different SPCE electrodes at a concentration of 5 fg/mL.

between Palmsens4-Simulation, and 0.9296 between Autolab-Simulation curves. The R^2 fit between instrument results was 0.9679 and 0.8915 for SenSARS-Autolab and SenSARS-PalmSens4, respectively, which in addition to portability and usability confirm the price-performance benefits of SenSARS for our application.

To verify the performance of our system with biological samples, we compared the EISs obtained for different SPCEs incubated with liquid samples at specific spike protein concentrations using SenSARS, Autolab, and Palmsens4 potentiostats, under equal settings (Fig. 11(a) and Table I).

Fig. 11(a) shows the EIS test results performed by SenSARS, Palmsens4, and Autolab systems for different electrodes, each functionalized up to BSA and with an incubated PBS fluid matrix sample at a concentration of 5 fg/mL of SARS-CoV2(S) antigen. Fig. 11(b) shows the equivalent percentage change in R_{ct} from each pair of BSA and antigen curves. The changes in R_{ct} values (ΔR_{ct}) were calculated by subtracting the R_{ct} values of BSA electrode from that functionalized with the spike protein.

Fig. 12(a) and (b) shows the SenSARS' linear response to incremental spike protein concentrations (numeric data can be found in Table S1). As the virus' concentration in the sample increases (i.e., spike protein content), the charge transfer resistance (R_{ct}) at the electrode's interface also increases.

In terms of analytical sensitivity, SenSARS' LOD was determined to be 1.065 fg/mL, from the mean of five blanks, their standard deviation, and the slope (analytical sensitivity) of the calibration plot (Fig. 12(b) and Table S1), at a confidence factor of 99%. Table S1 shows the tabulated results for three separate SPCE tests over five different spike protein

TABLE III
KEY BENEFITS OF SENSARS VERSUS OTHER TECHNOLOGIES

Properties	SenSARS	RT-PCR	[45]	[46]	[47]	[48]	[49]	[50]	[51]
Viral sample manipulation	NO	YES	YES	YES	YES	YES	NO	NO	NO
Requires trained personal*	NO	YES	NO	YES	YES	YES	YES	YES	YES
Requires specialized laboratories*	NO	YES	NO	YES	YES	YES	NO	YES	NO
Degree of manual sample processing	5%	75 %	0%	> 70 %	> 70%	> 70%	30%	50 %	30%
Time to results	~10 min	2-3 h	30 min	> 30 min	> 30 min	21 min	NA	15 min	30 min
LOD	77 virions (1 fg/ml)	100 virions	10^2-10^3 viruses/ml	10 ng/ml	1 copy/µl	0.1 µg/ml	15 fM	5 nM	8 ng/ml
Type of samples	AS, HO, or SA	AS, HO, or SA	AS, HO or SA	Human serum	AS, HO or SA	Cells	AS, HO or SA	Human serum	AS, HO or SA
Selective to	Antigen	RNA	Antigen	Antigen	RNA	RNA	Antigen	Antigen	Antigen
Price per test	< $5	$100	> $10	$8	> $10	> $10	NA	NA	> $10
TRL	TLR 7	TLR 9	TLR 6	TRL4	TLR 9	NA	TRL4	TRL4	NA
Pathogen adaptability	YES	YES	YES	YES	YES	NO	YES	YES	YES
Specificity	>90 %	>96 %	>90 %	>90 %	>90 %	NA	NA	NA	NA
Negative control to other pathogens	YES (EPV, H1N1, rhino)	NA	NA	NA	YES	YES	YES (S1, BSA, E2 HCV, CD48)	YES	YES
Mass producible	YES	YES	YES	NO	NO	NO	YES	YES	NO
Portable	YES	NO	YES	NO	NO	NO	YES	YES	YES
EMI electrode protection	YES	NO	YES	NO	NO	NO	NO	NO	NO
Standalone System+	YES	YES	YES	NO	NO	NO	NO	YES	NO

*For usage, not production. +No external devices required for detection. AS: nasopharyngeal aspirate, HO: nasopharyngeal swab, SA: Saliva, NA: not available.
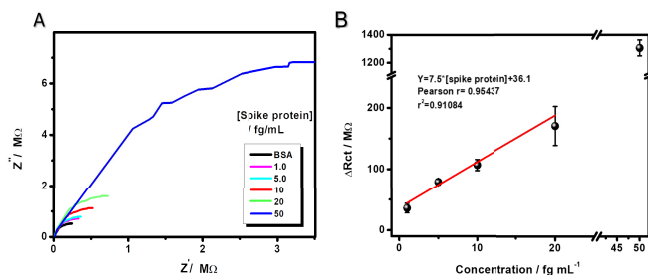

Fig. 12. (a) Relative EIS between incremental spike protein concentrations in a fluid sample. (b) Linear response in concentration versus ΔR_{ct} change between 1 and 20 fg/mL.

Fig. 13. Relative ΔR_{ct} values' comparison for incremental spike protein concentrations and negative control tests.

concentrations, i.e., 1, 5, 10, 20, and 50 fg/mL, from which the LOD and LOQ can be reproduced.

To confirm the analytical selectivity of SenSARS to SARS-CoV-2, the EIS was recorded on one electrode incubated with influenza virus (H1N1) and with Epstein–Barr virus (EBV), at 10 and 20 fg/mL dissolved in PBS 1X, 0.01 M at pH 7.4. As expected, no significant changes in R_{ct} are observed (Fig. 13 and Fig. S3) given there should be no cross-reactions between antigens from H1N1 and EBV and the anchored anti-spike-mAbs.

The time to diagnosis using the SenSARS system is approximately 10 min, of which 7 corresponds to the acquisition of electrode response signals to the ac potential excitations (Fig. 8) and less than 3 min to the EIS calculation. This assumes that the disposable SPCE has been previously characterized with a blank solution after bio-modification, and the corresponding EIS is available to compute the relative change in R_{ct}. This is a significant improvement over RT-PCR diagnostics, i.e. 2–3 h [8].

IV. DISCUSSION

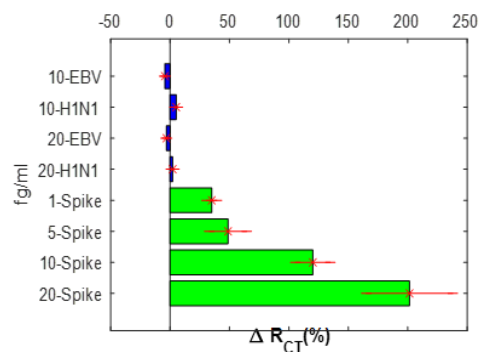SenSARS is a portable and standalone device that does not require any external device to operate. The overall cost of this instrument is <U.S. $200 (including manufacturing and assembly costs), while the estimated cost per bio-modified SPCE is under U.S. $5. With a diagnostic time under 10 min, an LOD of 1.065 fg/mL, an LOQ of 3.6 fg/mL (considering 10 times the standard deviation of the blank divided by its sensitivity), a high analytical selectivity (verified for influenza and EBV cross-reactions), and a linear calibration curve between 1 and 20 fg/mL, SenSARS should enable ubiquitous, rapid, early, and accurate detection of SARS-CoV-2 infections, as well as tracking viral load over tendencies time, thereby addressing some of the salient challenges in the diagnosis of this disease [53], [54]. An important issue that needs to be addressed in developing this technology further involves reducing inhomogeneities from the manual bio-modification of the SPCEs, as evidenced from the error bars in the calibration curves (Figs. 11(b) and 13). To this end, we propose using finer grain carbon-based paste for the SPCE thick-film screen printing, along with a pipetting robot or a liquid-handling station with a Peltier-controlled SPCE sheet holder at 5°C and a multiplexed potentiostat configuration to automate the surface functionalization and characterization protocols;

increasing the number of Fc-anchored mAbs via intermediate ligands (e.g., protein A) to improve epitope binding and sensitivity; and preserving the SPCEs in a controlled humid environment, including protecting the RE in a saturated KCl solution, to reduce degradation by oxidation, contamination, and denaturing of bio-functional layers (SPCE characteristics were confirmed to be consistent up to one week). Furthermore, the planar interdigitated three-electrode configuration used in SenSARS requires special care when characterizing patient samples containing surfactants (e.g., Triton X-100) to denature any viral capsids in the samples. Surfactants lower the surface tension at the air–liquid interface of the WE, which can lead to contamination (spilling over) of the Ag/AgCl RE with chloride and other species from incubated human samples that dynamically alter the reference potential and therefore the EIS results. We are currently working on embedding microfluidic channels in the SPCEs to constrain the fluid samples to the WE surface during incubation.

Despite the variance, our results show that a relative increase in R_{ct} above 10%, measured to the clean bio-modified SPCE, is sufficient for accurate, highly sensitive, and selective measurement of SARS-CoV-2 antigens. In other words, strict SPCE repeatability is not necessary, albeit desirable.

To improve point-of-care testing (POCT) and home-testing (HT) capabilities with SenSARS, other price performance factors need to be considered. We are currently working toward replacing the LCD touch screen with an LED bar and a mechanical function/test button to reduce weight and costs; reducing the form factor and overall weight via surface mounted low-voltage electronics; and encapsulating the SPCE into a cartridge to effectively handle and safely dispose of hazardous biological materials (e.g. virus-containing fluids).

SenSARS' benefits are compared in Table III against RT-PCR and other antigen-based technologies.

V. Conclusion

We have demonstrated a rapid and accurate antigen-based test (~10 min) for SARS-CoV-2 detection and viral load tracking. SenSARS combines a portable (<200 g), battery-powered (5-hautonomy), low-cost (<U.S. $200) instrument and disposable bio-modified SPCEs (<U.S. $5), both of which are amenable to commercial massification. SenSARS' low LOD (estimated at ~77 virions) should enable early diagnosis of SARS-CoV-2 infections where pathogen concentrations in the body are still undetectable by other means, even in the presence of other viruses with similar pathologies (EBV and H1N1). Improved fabrication and bio-modification of SPCEs may be addressed by automated means and the use of microfluidic techniques. Yet, even in the absence of highly homogeneous electrodes, our results demonstrate that relative R_{ct} values can provide an accurate diagnosis of SARS-CoV-2 infections.

At the time of this submission, SenSARS has now been validated in a controlled clinical trial of $n = 60$. The results from a cohort of patients confirmed via RT-PCR, undiagnosed co-habitants of patients, and healthy subjects using oro/nasopharyngeal fluid and saliva samples are consistent with those reported here using recombinant fluid matrix samples. These results are beyond the scope of this article [55].

SenSARS is designed for compliance with the IEC 60601-1 standard for *in vitro* diagnostics (IVDs), albeit further work needs to be done for certification.

We expect technologies like SenSARS will enable frequent, rapid, and accurate screening of individuals at primary care facilities, point-of-care (POC) sites, and even at home (HT). This will, in turn, enable selective and individualized quarantining, reduce transmission rates, load-balance health care systems, improve epidemiological tracking and management, and most importantly, save lives as we gradually return to a new socioeconomic equilibrium.

References

[1] T. Singhal, "A review of coronavirus disease-2019 (COVID-19)," *Indian J. Pediatrics*, vol. 87, pp. 281–286, Apr. 2020.

[2] B. Pfefferbaum and C. S. North, "Mental health and the COVID-19 pandemic," *New England J. Med.*, vol. 383, no. 6, pp. 510–512, Aug. 2020.

[3] M. Nicola *et al.*, "The socio-economic implications of the coronavirus pandemic (COVID-19): A review," *Int. J. Surg.*, vol. 78, pp. 185–193, Jun. 2020.

[4] Y. S. Malik *et al.*, "Coronavirus disease pandemic (COVID-19): Challenges and a global perspective," *Pathogens*, vol. 9, no. 7, p. 519, Jun. 2020.

[5] Y.-W. Tang, J. E. Schmitz, D. H. Persing, and C. W. Stratton, "Laboratory diagnosis of COVID-19: Current issues and challenges," *J. Clin. Microbiol.*, vol. 58, no. 6, pp. 1–22, May 2020.

[6] W. Feng *et al.*, "Molecular diagnosis of COVID-19: Challenges and research needs," *Anal. Chem.*, vol. 92, no. 15, pp. 10196–10209, Aug. 2020.

[7] M. P. Cheng *et al.*, "Diagnostic testing for severe acute respiratory syndrome–related coronavirus 2," *Ann. Internal Med.*, vol. 172, no. 11, pp. 726–734, Jun. 2020.

[8] A. Tahamtan and A. Ardebili, "Real-time RT-PCR in COVID-19 detection: Issues affecting the results," *Exp. Rev. Mol. Diag.*, vol. 20, no. 5, pp. 453–454, May 2020.

[9] Y. Li *et al.*, "Stability issues of RT-PCR testing of SARS-CoV-2 for hospitalized patients clinically diagnosed with COVID-19," *J. Med. Virol.*, vol. 92, no. 7, pp. 903–908, Jul. 2020.

[10] S. Ahmed *et al.*, "Current advances in immunoassays for the detection of antibiotics residues: A review," *Food Agricult. Immunol.*, vol. 31, no. 1, pp. 268–290, Jan. 2020.

[11] E. Mohit, Z. Rostami, and H. Vahidi, "A comparative review of immunoassays for COVID-19 detection," *Exp. Rev. Clin. Immunol.*, vol. 17, no. 6, pp. 573–599, Jun. 2021.

[12] P. Mohankumar, J. Ajayan, T. Mohanraj, and R. Yasodharan, "Recent developments in biosensors for healthcare and biomedical applications: A review," *Measurement*, vol. 167, Jan. 2021, Art. no. 108293.

[13] D. Sadighbayan and E. Ghafar-Zadeh, "Portable sensing devices for detection of COVID-19: A review," *IEEE Sensors J.*, vol. 21, no. 9, pp. 10219–10230, May 2021.

[14] G. Seo *et al.*, "Rapid detection of COVID-19 causative virus (SARS-CoV-2) in human nasopharyngeal swab specimens using field-effect transistor-based biosensor," *ACS Nano*, vol. 14, no. 4, pp. 5135–5142, 2020.

[15] G. Qiu, Z. Gai, Y. Tao, J. Schmitt, G. A. Kullak-Ublick, and J. Wang, "Dual-functional plasmonic photothermal biosensors for highly accurate severe acute respiratory syndrome coronavirus 2 detection," *ACS Nano*, vol. 14, no. 5, pp. 5268–5277, May 2020.

[16] A. K. Kaushik *et al.*, "Electrochemical SARS-CoV-2 sensing at point-of-care and artificial intelligence for intelligent COVID-19 management," *ACS Appl. Bio Mater.*, vol. 3, no. 11, pp. 7306–7325, Nov. 2020.

[17] S. Behera *et al.*, "Biosensors in diagnosing COVID-19 and recent development," *Sensors Int.*, vol. 1, Nov. 2020, Art. no. 100054.

[18] A. Yakoh, U. Pimpitak, S. Rengpipat, N. Hirankarn, O. Chailapakul, and S. Chaiyo, "Paper-based electrochemical biosensor for diagnosing COVID-19: Detection of SARS-CoV-2 antibodies and antigen," *Biosensors Bioelectron.*, vol. 176, Mar. 2021, Art. no. 112912.

[19] R. M. Torrente-Rodríguez *et al.*, "SARS-CoV-2 RapidPlex: A graphene-based multiplexed telemedicine platform for rapid and low-cost COVID-19 diagnosis and monitoring," *Matter*, vol. 3, no. 6, pp. 1981–1998, Dec. 2020.

[20] D. P. Valencia and G. Cebrià n-torrejòn, "Electrochemical SARS-CoV-2 aptamer-based devices," *Arch. Org. Inorg. Chem. Sci.*, vol. 5, no. 1, pp. 654–657, 2021.

[21] A. Panahi, A. Hassanzadeh, and A. Moulavi, "Design of a low cost, double triangle, piezoelectric sensor for respiratory monitoring applications," *Sensore Bio-Sensing Res.*, vol. 30, Dec. 2020, Art. no. 100378.

[22] S. Chen and M. H. Shamsi, "Biosensors-on-chip: A topical review," *J. Micromech. Microeng.*, vol. 27, no. 8, Aug. 2017, Art. no. 083001.

[23] S. D. Bukkitgar, N. P. Shetti, and T. M. Aminabhavi, "Electrochemical investigations for COVID-19 detection—A comparison with other viral detection methods," *Chem. Eng. J.*, vol. 420, Sep. 2021, Art. no. 127575.

[24] A. M. Pernia, M. J. Prieto, I. C. Orille, J. A. Martin-Ramos, and A. Costa-Garcia, "Development of optimized screen-printed immunosensors," *IEEE Trans. Instrum. Meas.*, vol. 58, no. 7, pp. 2181–2188, Jul. 2009.

[25] S. Tonello *et al.*, "Wireless point-of-care platform with screen-printed sensors for biomarkers detection," *IEEE Trans. Instrum. Meas.*, vol. 66, no. 9, pp. 2448–2455, Sep. 2017.

[26] J. C. Fidler, W. R. Penrose, and J. P. Bobis, "A potentiostat based on a voltage-controlled current source for use with amperometric gas sensors," *IEEE Trans. Instrum. Meas.*, vol. 41, no. 2, pp. 308–310, Apr. 1992.

[27] A. V. Gopinath and D. Russell, "An inexpensive field-portable programmable potentiostat," *Chem. Educ.*, vol. 6, no. 5, pp. 1–6, 2005.

[28] J. R. Blanco, "Design of a low-cost portable potentiostat for amperometric biosensors," in *Proc. IEEE Instrum. Meas. Technol. Conf.*, Dec. 2006, pp. 690–694.

[29] O. V. Moskovkin, "A circuit for automatic compensation of the ohmic resistance of a solution in a three-electrode chemical cell by the current chopping method," *Instrum. Exp. Techn.*, vol. 43, no. 3, pp. 403–405, May 2000.

[30] C.-L. Hsu, T. Zhang, Y.-H. Lo, and D. A. Hall, "A low-noise gain-enhanced readout amplifier for induced molecular electronic signals," in *Proc. IEEE Biomed. Circuits Syst. Conf. (BioCAS)*, Oct. 2015, pp. 1–4.

[31] G. Ferrari, F. Gozzini, and M. Sampietro, "Transimpedance amplifiers for extremely high sensitivity impedance measurements on nanodevices," in *Analog Circuit Design*. Dordrecht, The Netherlands: Springe, 2006, pp. 193–207.

[32] G. Ferrari and M. Sampietro, "Wide bandwidth transimpedance amplifier for extremely high sensitivity continuous measurements," *Rev. Sci. Instrum.*, vol. 78, no. 9, Sep. 2007, Art. no. 094703.

[33] S. Dai and J. K. Rosenstein, "A dual-mode low-noise nanosensor front-end with 155-dB dynamic range," in *Proc. IEEE Biomed. Circuits Syst. Conf. (BioCAS)*, Oct. 2015, pp. 1–4.

[34] V. Bianchi, A. Boni, S. Fortunati, M. Giannetto, M. Careri, and I. De Munari, "A Wi-Fi cloud-based portable potentiostat for electrochemical biosensors," *IEEE Trans. Instrum. Meas.*, vol. 69, no. 6, pp. 3232–3240, Jun. 2020.

[35] A. Lasia, "Electrochemical impedance spectroscopy and its applications," in *Modern Aspects of Electrochemistry*, vol. 32, no. 32. Boston, MA, USA: Kluwer, 2002, pp. 143–248.

[36] C. Yang, D. Rairigh, and A. Mason, "On-chip electrochemical impedance spectroscopy for biosensor arrays," in *Proc. 5th IEEE Conf. Sensors*, Oct. 2006, pp. 93–96.

[37] E. P. Randviir and C. E. Banks, "Electrochemical impedance spectroscopy: An overview of bioanalytical applications," *Anal. Methods*, vol. 5, no. 5, p. 1098, 2013.

[38] M. C. Salvadori, D. R. Martins, and M. Cattani, "DLC coating roughness as a function of film thickness," *Surf. Coat. Technol.*, vol. 200, pp. 5119–5122, Apr. 2006.

[39] G. Bar, Y. Thomann, R. Brandsch, H.-J. Cantow, and M.-H. Whangbo, "Factors affecting the height and phase images in tapping mode atomic force microscopy. study of phase-separated polymer blends of poly(ethene-co-styrene) and poly(2,6-dimethyl-1,4-phenylene oxide)," *Langmuir*, vol. 13, no. 14, pp. 3807–3812, Jul. 1997.

[40] P. J. James, M. Antognozzi, J. Tamayo, T. J. Mcmaster, J. M. Newton, and M. J. Miles, "Interpretation of contrast in tapping mode AFM and shear force microscopy. A study of Nafion," *Langmuir*, vol. 17, no. 2, pp. 349–360, Jan. 2001.

[41] D. Nidzworski *et al.*, "A rapid-response ultrasensitive biosensor for influenza virus detection using antibody modified boron-doped diamond," *Sci. Rep.*, vol. 7, no. 1, p. 15707, Dec. 2017.

[42] M. Orlando, T. Ravasenga, E. M. Petrini, A. Falqui, R. Marotta, and A. Barberis, "Correlating fluorescence and high-resolution scanning electron microscopy (HRSEM) for the study of GABAA receptor clustering induced by inhibitory synaptic plasticity," *Sci. Rep.*, vol. 7, no. 1, pp. 1–10, Dec. 2017.

[43] H. M. Berman *et al.*, "The protein data bank," *Acta Crystallogr. D, Biol. Crystallogr.*, vol. 58, no. 6, pp. 899–907, Jun. 2002.

[44] N. F. Martinez *et al.*, "Bimodal atomic force microscopy imaging of isolated antibodies in air and liquids," *Nanotechnology*, vol. 19, no. 38, 2008, Art. no. 384011.

[45] G. Ruiz-Vega, M. Soler, and L. M. Lechuga, "Nanophotonic biosensors for point-of-care COVID-19 diagnostics and coronavirus surveillance," *J. Phys., Photon.*, vol. 3, no. 1, Jan. 2021, Art. no. 011002.

[46] Z. Zhang *et al.*, "Multiplex quantitative detection of SARS-CoV-2 specific IgG and IgM antibodies based on DNA-assisted nanopore sensing," *Biosensors Bioelectron.*, vol. 181, Jun. 2021, Art. no. 113134.

[47] T. Chaibun *et al.*, "Rapid electrochemical detection of coronavirus SARS-CoV-2," *Nature Commun.*, vol. 12, no. 1, p. 802, Dec. 2021.

[48] L.-V. Kiew *et al.*, "Development of flexible electrochemical impedance spectroscopy-based biosensing platform for rapid screening of SARS-CoV-2 inhibitors," *Biosensors Bioelectron.*, vol. 183, Jul. 2021, Art. no. 113213.

[49] A. Raziq, A. Kidakova, R. Boroznjak, J. Reut, A. Öpik, and V. Syritski, "Development of a portable MIP-based electrochemical sensor for detection of SARS-CoV-2 antigen," *Biosensors Bioelectron.*, vol. 178, Apr. 2021, Art. no. 113029.

[50] S. Kim *et al.*, "Vertical flow cellulose-based assays for SARS-CoV-2 antibody detection in human serum," *ACS Sensors*, vol. 6, no. 5, pp. 1891–1898, May 2021.

[51] L. Fabiani *et al.*, "Magnetic beads combined with carbon black-based screen-printed electrodes for COVID-19: A reliable and miniaturized electrochemical immunosensor for SARS-CoV-2 detection in saliva," *Biosensors Bioelectron.*, vol. 171, Jan. 2021, Art. no. 112686.

[52] A. S. Bondarenko and G. A. Ragoisha, *Progress in Chemometrics Research*, A. L. Pomerantsev, Ed. New York, NY, USA: Nova Science Publishers, 2005, pp. 89–102.

[53] M. Ezhilan, I. Suresh, and N. Nesakumar, "SARS-CoV, MERS-CoV and SARS-CoV-2: A diagnostic challenge," *Measurement*, vol. 168, Jan. 2021, Art. no. 108335.

[54] A. Yassine, "Health monitoring systems for the elderly during COVID-19 pandemic: Measurement requirements and challenges," *IEEE Instrum. Meas. Mag.*, vol. 24, pp. 6–12, 2021.

[55] O. L. Agudelo *et al.*, "Clinical diagnostic performance of a carbon-based immunoreaction-based biosensor for the detection of SARS-CoV-2 infection," *J. Infectious Diseases*, Oct. 2021.

Sammy A. Perdomo received the B.S. degree in electronic engineering and the M.S. degree in industrial control engineering from the University of Ibagué, Ibagué, Colombia, in 2014 and 2016, respectively. He is currently pursuing the Ph.D. degree in engineering and applied sciences with Pontificia Universidad Javeriana Cali, Bogota, Colombia.

Viviana Ortega received the B.S. degree in chemistry from the Universidad del Valle, Cali, Colombia, in 2017, where she is currently pursuing the master's degree in chemistry.

During the last years, she has worked on the synthesis and characterization of catalysts for applications in subjects of clinical and industrial interest.

Andres Jaramillo-Botero received the B.S. degree in electrical engineering from Boston University, Boston, MA, USA, in 1986, the M.S. degree in computer science as a Fulbright Scholar from the State University of New York, Albany, NY, USA, in 1990, and the Ph.D. degree in engineering from the Polytechnic University of Valencia, Valencia, Spain, in 1998.

He completed his dissertation as a Visiting Research Fellow at the California Institute of Technology (Caltech), Pasadena, CA, USA, and NASA's Jet Propulsion Laboratory (JPL). He did postdoctoral work in nanoscale science as an NSF Fellow at Caltech and the Institute for Pure and Applied Mathematics, University of California, Los Angeles, CA. He joined Caltech in 2006, as Research Scientist and Lecturer in the Division of Chemistry and Chemical Engineering, and as the Director of Multiscale Science in the Center for Materials and Process Simulation. He is an elected member of the Honor Society of the Pontificia Universidad Javeriana (PUJ) in Colombia (since 2001), and the Scientific Director of the international research program ÓMICAS, Colombian scientific ecosystem, anchored at PUJ, Cali. His work includes contributions to nonadiabatic dynamics of molecules and materials, hypervelocity impact dynamics, low-temperature material growth, nanodevices and nanosensors, and nanoscale modeling, simulation, and control.

Nelson Mancilla received the B.S. degree in chemistry from the University of Valle, Cali, Colombia, in 2007, and the master's degree in engineering with Pontificia Universidad Javeriana, Bogota, Colombia, in 2021.

José Hernando Mosquera-DeLaCruz received the B.S. degree in electronics engineering from the Universidad del Valle, Cali, Colombia, in 2015. He is currently pursuing the Ph.D. degree in engineering from the Pontificia Universidad Javeriana Cali, Bogota, Colombia.

Drochss Pettry Valencia received the Ph.D. degree in chemical science in CINVESTAV-IPN in 2012.

His interest focuses on molecular electrochemistry and bio-electrochemical surfaces, supramolecular and materials electrochemistry, and electrochemistry of carbon nanostructures.

Mauricio Quimbaya received the B.S. degree in biology from the Universidad Nacional de Colombia, Bogota, Colombia, in 2004, and the Ph.D. degree in biotechnology from Ghent University, Ghent, U.K., in association with the Vlaams Instituut voor Biotechnologie (VIB), Flanders, Belgium, in 2011.

He is currently an Associate Professor at Pontificia Universidad Javeriana Cali, Bogota. His main research areas are focused on comparative genomics applied to cancer and plants research.

Juan David Contreras received the B.S. degree in mechanical engineering and the M.S. degree in engineering from Universidad del Valle Cali, Cali, Colombia, in 2014 and 2017, respectively.

He is currently a Lecturer and the Coordinator of the Process Automation Center, Pontificia Universidad Javeriana Cali, Bogota, Colombia.

Gabriel Esteban Vélez received the B.S. degree in chemistry from Universidad del Valle, Cali, Colombia, in 2013. He is currently pursuing the M.S. degree in biotechnology with ICESI University, Cali.

Oscar A. Loaiza received the B.S. degree in chemistry from the Universidad del Quindío, in 2001, and the Ph.D. degree from the Universidad Complutense de Madrid, Madrid, Spain.

He did postdoctoral work in electrochemical biosensors in Universidad del Valle, Cali, Colombia, from 2015 to 2020. In 2020, he joined the company Biolan biosensors through a Marie Sklodoska Curie grant.

Adriana Gómez received the B.S degree in mechanical engineering from the National University of Colombia, Bogota, Spain, in 2000, and the Ph.D. degree in materials and metallurgical engineering from the University of São Paulo, São Paulo, Brazil, in 2010.

She did postdoctoral work on characterization of thin films at the Surface Phenomena Laboratory, University of São Paulo. She is currently an Associate Professor at Pontificia Universidad Javeriana in Colombia. Her research interests include materials characterization and determination of residual stress of thin films by Xray diffraction techniques.

Jhonattan de la Roche received the B.S. degree in materials engineering from Universidad del Valle, Cali, Colombia, in 2010, the M.S. degree in science-physics from Universidad Nacional de Colombia, Bogota, Colombia, in 2014, and the Ph.D. degree in engineering-materials science and technology from the Universidad Nacional de Colombia, in 2020.

He is currently doing his postdoctoral stay in the ÓMICAS program at the Pontificia Universidad Javeriana Cali, Cali.